Merons in strained PbZr$_{0.2}$Ti$_{0.8}$O$_3$ thin films: Insights from phase-field simulations

Xujing Li,[1] Houbing Huang,[2] Fengxia Hu,[1,3,4] Jian-Tao Wang ⊕,[1,3,4,*] and Changfeng Chen[5]

[1]*Beijing National Laboratory for Condensed Matter Physics and Institute of Physics, Chinese Academy of Sciences, Beijing 100190, China*
[2]*Advanced Research Institute of Multidisciplinary Science, Beijing Institute of Technology, Beijing 100081, China*
[3]*School of Physical Sciences, University of Chinese Academy of Sciences, Beijing 100049, China*
[4]*Songshan Lake Materials Laboratory, Dongguan, Guangdong 523808, China*
[5]*Department of Physics and Astronomy, University of Nevada, Las Vegas, Nevada 89154, USA*

Materials exhibiting nontrivial topological spin textures known as merons attract considerable interest for their fascinating underlying physics and promising device applications. The PbTiO$_3$ family of compounds is known to host ferroelectric, ferroelastic, and piezoelectric polar orders and possess topological domain structures that are sensitive to external conditions. Here, we examine the polar states in PbZr$_{0.2}$Ti$_{0.8}$O$_3$ (PZT) thin films and explore the influence of film thickness and epitaxial strain via phase-field modeling under short-circuit (sc) and open-circuit (oc) boundary conditions. In this paper, we uncovered four distinct meron states in ultrathin films with tensile strains. Under the sc boundary condition, there is an intermediate meron bubble texture comprising a twisted Néel-like and Bloch-like meron texture with a distinct helicity and a meron bubble pair texture combining two intermediate merons along the z axis. Under the oc boundary condition, there is an antimeron bubble texture with negative winding numbers and an achiral topology, and a trimeron bubble texture with two antimeron bubbles and one meron bubble. These simulation results show that strain and film thickness have a major impact on the polarization strength and topology to dictate the formation and transition of meron phases in PZT thin films. The insights obtained in this paper may help elucidate and design materials with tailored and tunable microscopic and mesoscopic polar topological structures.

DOI: 10.1103/PhysRevB.109.094116

I. INTRODUCTION

Topologically nontrivial polar structures hold major significance in materials research due to their fascinating underlying physics and exciting potentials for application in next-generation memory devices and sensors [1–4]. Concerted efforts have been made to understand, design, and manipulate different kinds of topological defects, such as vortices [5–8], antivortices [9,10], flux-closures [11–13], skyrmions [14–18], merons [19,20], and their variants [4] in nanocomposites, low-dimensional ferroelectric films, superlattices, and liquid crystals. The nontrivial topological textures observed in ferroelectric materials share similarities with magnetic systems [21–27]. However, the mechanisms responsible for the formation of these topological structures are distinct from those in ferromagnetic and ferroelectric systems. For magnetic systems, Dzyaloshinskii-Moriya (DM) interaction provides out-of-plane coupling components for spins, and the continuous spin rotation creates skyrmions. Meanwhile, the interplay between elastic and electrostatic energies creates a delicate balance to allow spontaneous emergence of nontrivial topological polar textures in ferroelectric systems [15,19]. As a result, topological textures in ferroelectric materials can be manipulated by a wide array of external conditions, such as electric fields, strains, optical effects, and temperature [1,2].

In recent years, the emergence of polar topological textures has been demonstrated in ferroelectric films and superlattices of PbTiO$_3$ (PTO) derived systems. The presence of flux-closure structures was observed in PbZr$_{0.2}$Ti$_{0.8}$O$_3$ (PZT) thin films grown on SrTiO$_3$ (STO) substrates, with a SrRuO$_3$ (SRO) marker layer inserted at the PZT/STO interface [11]. Subsequently, by choosing different substrates, skyrmion-related polar topological structures were created in PZT systems [14–16,28]. More recently, polar meron and antimeron lattices were observed in PTO/SSO ferroelectric thin films on an orthorhombic SmScO$_3$ (SSO) substrate with a very small lattice mismatch of 0.5% tensile strain [20]. Moreover, polar antivortices were observed in the STO layer [9] driven by the boundary effects in [PTO]$_n$/[STO]$_n$ superlattices. To understand these rich experimental phenomena and elucidate the underlying mechanisms, it is necessary to clarify the origin of these polar textures and establish relevant phase diagrams. For this purpose, the approach of phase-field modeling is a powerful tool to explore and predicate the evolution of ferroelectric domains, phase transitions, domain wall variations, and topological texture changes, under different external conditions [14,26,29–32]. It has been shown that film thickness [33,34], strain [35], boundary condition [36], and external field [5,28,37,38] are effective in tuning domain patterns.

In this paper, we report on an in-depth study of the polar topology in PZT thin films, using the phase-field modeling approach, to construct phase diagrams for the evolution of polar topological texture driven by the changes in film

---

*Corresponding author: wjt@aphy.iphy.ac.cn

thickness and strain. Our results identify 14 states, among which four are distinct topologically nontrivial phases, including an intermediate meron bubble phase, a meron bubble pair phase, a trimeron bubble phase, and an antimeron bubble phase, under short-circuit (sc) or open-circuit (oc) boundary conditions. The trimeron bubble phase consists of two antimeron bubbles and one meron bubble in-plane. Meanwhile, the meron pair phase adopts a diabolo shape with two chiral inversion intermediate meron bubbles (I-meron). The divergent and convergent structures of the meron pairs coexist in PZT ultrathin films. These states exhibit strong sensitivity to film thickness, which drive phase transformations. The findings from these simulations enhance the understanding of mechanisms generating and driving changes in these polar topological textures and provide guidance for their experimental identification and manipulation.

II. METHOD AND MODELING

Our phase-field simulations were performed based on the thermodynamic Ginzburg-Landau-Devonshire (GLD) model for a ferroelectric system [39–42]. Application of the phenomenological GLD model permits calculations of strain-thickness phase diagrams for polarization. Here, we consider a ferroelectric film comprising three layers with different compositions: a PZT thin film, a substrate, and an air layer. The total free energy of the ferroelectric film includes Landau free energy (f_L), gradient energy (f_g), elastic energy ($f_{elastic}$), and electrostatic energy (f_{elec}). The total free energy density functional is

$$f(P, P_{i,j}, \varepsilon) = f_L + f_g + f_{elastic} + f_{elec}. \tag{1}$$

In the context of the Landau phase transition theory, the order parameter is zero on the high-temperature side and nonzero on the low-temperature side of the phase transition. The Landau free energy density in the sixth order polynomial is given by

$$
\begin{aligned}
f_L = {}& \alpha_1(T)\left(P_1^2 + P_2^2 + P_3^2\right) + \alpha_{11}\left(P_1^4 + P_2^4 + P_3^4\right) \\
& + \alpha_{12}\left(P_1^2 P_2^2 + P_1^2 P_3^2 + P_2^2 P_3^2\right) + \alpha_{111}\left(P_1^6 + P_2^6 + P_3^6\right) \\
& + \alpha_{112}\left[P_1^4\left(P_2^2 + P_3^2\right) + P_2^4\left(P_1^2 + P_3^2\right) \right. \\
& \left. + P_3^4\left(P_1^2 + P_2^2\right)\right] + \alpha_{123}\left(P_1^2 P_2^2 P_3^2\right).
\end{aligned} \tag{2}
$$

The Landau constants α_{ijk} are measured and calculated under the stress-free condition. The gradient energy density, which accounts for the energy of domain walls and the inhomogeneous spatial distribution of polarization, is given by

$$f_g = \tfrac{1}{2} G_{ijkl} P_{i,j} P_{k,l}, \tag{3}$$

where G_{ijkl} is a gradient energy constant, and $P_{i,j} = \frac{\partial P_i}{\partial x_j}$ means the partial derivative of polarization to displacement. For a cubic system under high temperature, the coefficients of the gradient energy only retain three independent components. Using the Voigt symbol simplification, the gradient matrix is

shown as

$$
G = \begin{pmatrix}
G_{11} & G_{12} & G_{12} & 0 & 0 & 0 \\
G_{12} & G_{11} & G_{12} & 0 & 0 & 0 \\
G_{12} & G_{12} & G_{11} & 0 & 0 & 0 \\
0 & 0 & 0 & G_{44} & 0 & 0 \\
0 & 0 & 0 & 0 & G_{44} & 0 \\
0 & 0 & 0 & 0 & 0 & G_{44}
\end{pmatrix}. \tag{4}
$$

Nambu and Sagala [41] revised the gradient energy, making it more precise as

$$
\begin{aligned}
f_g = {}& \frac{1}{2} G_{11}\left(P_{1,1}^2 + P_{2,2}^2 + P_{3,3}^2\right) \\
& + G_{12}(P_{1,1}P_{2,2} + P_{2,2}P_{3,3} + P_{3,3}P_{1,1}) + \left(\frac{G_{44} + G_{44}'}{2}\right) \\
& \times \left(P_{1,2}^2 + P_{2,1}^2 + P_{2,3}^2 + P_{3,2}^2 + P_{1,3}^2 + P_{3,1}^2\right) \\
& + (G_{44} - G_{44}')(P_{1,2}P_{2,1} + P_{1,3}P_{3,1} + P_{2,3}P_{3,2}).
\end{aligned} \tag{5}
$$

The elastic energy density $f_{elastic}$ is defined as

$$f_{elastic} = \tfrac{1}{2} C_{ijkl}\left(\varepsilon_{ij} - \varepsilon_{ij}^0\right)\left(\varepsilon_{kl} - \varepsilon_{kl}^0\right), \tag{6}$$

where C_{ijkl} is the elastic constant, and ε_{ij}^0 is the stress-free transformation strain or eigenstrain. The strain solution satisfies the boundary conditions and mechanical equilibrium $\frac{\partial \sigma_{ij}}{\partial x_j} = 0$. The elastic energy is given by the multiplication of the elastic stress $\sigma_{ij} = C_{ijkl}(\varepsilon_{ij} - \varepsilon_{ij}^0)$, with the elastic strain $\varepsilon_{ij} - \varepsilon_{ij}^0$. The elastic strain is the total strain ε_{ij} subtracted by the stress-free heterogeneous strain ε_{ij}^0. The total strain ε_{ij} is given as $\varepsilon_{ij} = \bar{\varepsilon}_{ij} + \eta_{ij}$, where $\bar{\varepsilon}_{ij}$ is the homogeneous strain, and η_{ij} is the heterogeneous strain, which satisfies the condition $\int_V \eta_{ij} dV = 0$. If $\bar{\varepsilon}_{ij}$ represents the macroscopic shape deformation of the thin film, $\bar{\varepsilon}_{11} = \bar{\varepsilon}_{22} = \frac{a_{sub} - a_{lattice}}{a_{lattice}}$, $\bar{\varepsilon}_{12} = \bar{\varepsilon}_{21} = 0$. The thin film mechanical boundary conditions correspond to a strain-free bottom ($u_i|_{x_3 = h_{sub}} = 0$) and a stress-free surface ($\sigma_{i3}|_{x_3 = h_{film}} = 0$) [42]. The eigenstrain is related to polarization as

$$
\begin{aligned}
\varepsilon_{11}^0 &= Q_{11}P_1^2 + Q_{12}\left(P_2^2 + P_3^2\right), \\
\varepsilon_{22}^0 &= Q_{11}P_2^2 + Q_{12}\left(P_3^2 + P_1^2\right), \\
\varepsilon_{33}^0 &= Q_{11}P_3^2 + Q_{12}\left(P_1^2 + P_2^2\right), \\
\varepsilon_{23}^0 &= Q_{44}P_2 P_3, \\
\varepsilon_{13}^0 &= Q_{44}P_1 P_3, \\
\varepsilon_{12}^0 &= Q_{44}P_1 P_2,
\end{aligned} \tag{7}
$$

where Q_{ij} are electrostrictive coefficients.

The electrostatic energy density f_{elec} is based on the energy generated by the interaction between the polarization vector and the electric field, which is divided into three items. The first term contributes to the dipole-dipole interaction (which is self-energy term), and the second term contributes to the depolarization field (this is caused by the uncompensated surface charge). The third term contributes to the applied electric field. This energy density is given by

$$f_{elec} = -\tfrac{1}{2} E_i^{dip} P_i - \tfrac{1}{2} E_i^{dep,surf} \bar{P}_i - E_i^{app} P_i, \tag{8}$$

TABLE I. Parameters of Landau coefficient, electrostrictive coefficient, elastic coefficient, and gradient energy [47].

Parameter	Value	Unit (SI)
α_1	$3.44(\,T - 729.5)$	$(10^5)\text{m}^2\text{N/C}^2$
α_{11}	-3.05	$(10^7)\text{m}^6\text{N/C}^4$
α_{12}	6.32	$(10^8)\text{m}^6\text{N/C}^4$
α_{111}	2.47	$(10^8)\text{m}^{10}\text{N/C}^6$
α_{112}	9.68	$(10^8)\text{m}^{10}\text{N/C}^6$
α_{123}	-4.9	$(10^9)\text{m}^{10}\text{N/C}^6$
Q_{11}	8.1	$(10^{-2})\text{m}^4\text{/C}^2$
Q_{12}	-2.4	$(10^{-2})\text{m}^4\text{/C}^2$
Q_{44}	3.2	$(10^{-2})\text{m}^4\text{/C}^2$
C_{11}	1.746	$(10^{11})\text{Pa}$
C_{12}	0.7937	$(10^{11})\text{Pa}$
C_{44}	1.111	$(10^{11})\text{Pa}$
G_{110}	1.73	$(10^{-10})\text{m}^4\text{N/C}^2$
G_{11}	$0.6G_{110}$	$(10^{-10})\text{m}^4\text{N/C}^2$
G_{12}	$0G_{110}$	$(10^{-10})\text{m}^4\text{N/C}^2$
G_{44}	$0.6G_{110}$	$(10^{-10})\text{m}^4\text{N/C}^2$

where E_i^{dip} is induced by the dipole-dipole interaction, $E_i^{\text{dep,surf}}$ is the depolarization field which is from the dipole-dipole interactions but also the long-range electrostatic interaction, and E_i^{app} is the externally applied electric field. Here, $\bar{P}_i$ is the spatial average of the ith component of polarization.

The electric displacement D_i is related to the electric field as $D_i = \epsilon_0 \kappa_{ij} E_j^d + P_i$, where κ_{ij} is the relative dielectric permittivity of the ferroelectric film. The electrostatic equilibrium equations of the film can be described by $D_{i,i} = 0$ ($D_{i,j} = \frac{\partial D_i}{\partial x_j}$) with the boundary conditions $D_3|_{x_3=h_{\text{sub}}, h_{\text{film}}} = 0$ for an oc and $\phi|_{h_{\text{sub}}} = \phi_1, \phi|_{h_{\text{film}}} = \phi_2$ for a sc [43,44]. Accounting for the interplay between thickness, strain, and boundary condition is necessary to correctly determine the topology of the polar textures.

In the phase-field model, temporal evolution of polarization is described by the time-dependent Ginzburg-Landau (TDGL) equation:

$$\frac{\partial P_i(\vec{r}, t)}{\partial t} = -L \frac{\delta F}{\delta P_i(\vec{r}, t)}, \qquad (9)$$

where L is the kinetic coefficient related to the domain wall mobility, and F is total free energy. We employed the semi-implicit Fourier spectral method [45] for both time and spatial discretization to solve the TDGL equation, adopting the correlated origin codes by Gu *et al.* [46] using MATLAB. The initial system is in a random state, which describes the paraelectric phase. Polarization is in the nonzero range for the film and in the zero range for the air space and substrate layer. The parameters of the Landau coefficient, gradient energy, elastic coefficient, and electrostrictive coefficient [47] are listed in Table I. Periodic boundary conditions are applied along the x and y directions. The grid spaces in real space along

the three directions are $\Delta x = \Delta y = 2.5 * \Delta z = l_0$. The grid length $l_0 = \sqrt{G_{110}/a_0}$. The revolution of each step dt is 2.37×10^{-13}s $[dt = 0.01/L\alpha_0]$, where $\alpha_0 = \alpha_1(T = 298\,\text{K})$, $L = 3 \times 10^4$ C^2/Nm^{2}s [48]. Here, $64 \times 64 \times h$ (h corresponds to the thickness of the PZT film layer) defines the discrete grid in the PZT films, and $64 \times 64 \times 10$ describes the individual sites for the various substrates.

III. RESULTS AND DISCUSSION

A. Polar skyrmion and meron patterns

The topological characters of the textured domains are defined by topological charge, also called skyrmion number [1,21], which can be calculated via the closed-loop integral of the vector field angle:

$$N_{\text{sk}} = \frac{1}{4\pi} \iint \mathbf{P} \cdot \left(\frac{\partial \mathbf{P}}{\partial x} \times \frac{\partial \mathbf{P}}{\partial y} \right) dx\,dy, \qquad (10)$$

where $\mathbf{P}$ is the polarization. Using the symmetry of the skyrmion [21], one can write $\mathbf{P}(\mathbf{r}) = [\sin\theta(r)\cos\phi, \sin\theta(r)\sin\phi, \cos\theta(r)]$, with $\phi(\varphi) = m\varphi + \gamma$. The topological charge density [24], also called Pontryagin density (ρ), is given by $\rho = \mathbf{P} \cdot (\frac{\partial \mathbf{P}}{\partial x} \times \frac{\partial \mathbf{P}}{\partial y})$.

To understand various skyrmionlike textures, the images of Bloch-like and Néel-like skyrmions are shown in Figs. 1(a)–1(d) and those of merons in Figs. 1(e)–1(h), with the out-of-plane polarization components (P_{op}) and in-plane polarization components (P_{ip}). It is seen in Figs. 1(a)–1(d) that P_{op} appears at the core (red up arrows) and an antiparallel P_{op} outside the boundary (blue down arrows) for skyrmions. The distinction between the Bloch-like and Néel-like skyrmions lies in their helicity (γ), where the polarization rotates in the plane [21], as $\gamma = 0, \pm\pi/2$ or π. The $m = \pm 1$ means vorticity. The polarization configurations of the vortices can be described by $\phi(\varphi)$, which is the angle between the x axis and the polarization vector at one point with the angle φ along a loop around the vortex core [10].

The Néel-like skyrmion is shown in Fig. 1(a) with achiral characters [49]. The polarization continuously rotates in such a way that P_{ip} exhibits a curling Néel domain wall and converges toward the central core, as shown in Fig. 1(a). The Bloch-like skyrmion is shown in Fig. 1(c) with counterclockwise vortex and right-handedness chirality [6,19]. Here, P_{ip} exhibits a curling Bloch domain wall. The antiskyrmions are achiral [19,49], as shown in Figs. 1(b) and 1(d). A common feature of both Bloch ($\nabla \times P \neq 0$) and Néel ($\nabla \cdot P \neq 0$) skyrmions is that the out-of-plane polarization rotates from maximal at the core to maximal in the opposite direction at the periphery. Meanwhile, the meron [Figs. 1(e)–1(h)] exhibits P_{op} only at the core and gradually evolves to P_{ip} at the boundary, without being fully surrounded by an antiparallel P_{op} component. As an example, shown in Figs. 1(a) and 1(e) are a skyrmion and a meron (half of skyrmion) that can have the same P_{ip} texture, vorticity, and helicity but have varied P_{op} components at the periphery.

B. Phase diagram and polar topologies

To understand the evolution of different topological textures under varying film thickness (h) and strain (S), we
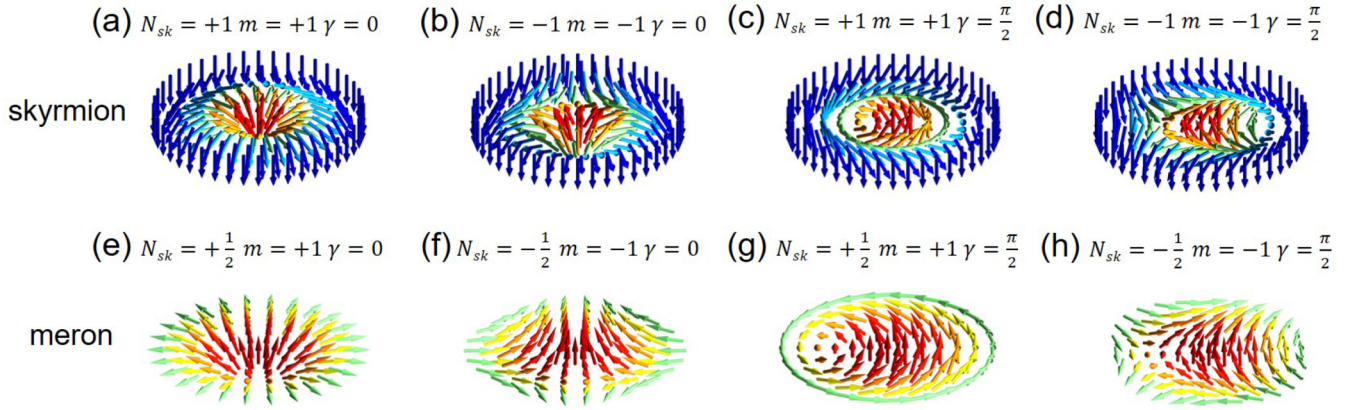
FIG. 1. Sketches of the dipolar textures for skyrmions vs merons. (a) The Néel-like skyrmion with $N_{sk} = +1$, $m = +1$, and $\gamma = 0$. (b) The antiskyrmion with $N_{sk} = -1$, $m = -1$, and $\gamma = 0$. (c) The Bloch-like skyrmion with $N_{sk} = +1$, $m = +1$, and $\gamma = \pi/2$. (d) The antiskyrmion with $N_{sk} = -1$, $m = -1$, and $\gamma = \pi/2$. Here, N_{sk} is topological charge, m is topological vorticity (winding number), and γ is helicity. The Bloch-like skyrmion in (c) has right-handed chirality. (e) and (f) are Néel-like meron and antimeron, with $N_{sk} = +\frac{1}{2}$, $m = +1$, and $\gamma = 0$ and $N_{sk} = -\frac{1}{2}$, $m = -1$, and $\gamma = 0$, respectively. (g) and (h) are Bloch-like meron and antimeron, $N_{sk} = +\frac{1}{2}$, $m = +1$, and $\gamma = \pi/2$ and $N_{sk} = -\frac{1}{2}$, $m = -1$, and $\gamma = \pi/2$, respectively. The topological character of the meron is half that of the skyrmion with topological charge $N_{sk} = \frac{1}{2}$.

constructed an h-S phase diagram for PZT film via phase-field modeling. We set different electric boundary conditions to simulate the effects induced by a SRO or STO marker layer with a nominal thickness of 1.5 u.c. [11] at the PZT/STO interface. The SRO layer corresponds to the sc boundary condition, while the STO layer corresponds to the oc boundary condition. We have simulated the domain structures with varying epitaxial strain ranging from −2 to 2% and film thickness ranging from 2 to 40 u.c. under sc and oc boundary conditions. The initial domain textures with zero strain are shown in Fig. S1 in the Supplemental Material [50].

Under the sc boundary condition, as shown in Fig. 2(a), we find eight states in the h-S phase diagram. They are (1) the c stripe domain with a 180° domain wall, and the domain for a mismatch strain of $\varepsilon_{11} = -1\%$ is shown in Fig. 3(a) that has no topological texture [Fig. 3(e)] at high compressive strains at any thickness [51]; (2) the c zigzag stripe domain that is a variant of the c stripe domain in thick films, but the domain walls along the z axis are zigzag shaped in the cross-section [52]; (3) the c/a stripe domain at small strains and large thicknesses, for which the polarization exits aligned along both the in-plane [100] and out-of-plane [001] directions, and can exist in the bulk [53]; and (4) the a_1/a_2 stripe state emerges under large tensile strains with 90° domain walls, which is opposite to the c stripe state observed under compressive strain, and the polarization direction aligns with the [100] and [010] axes [42]. These four states have already been reported in PZT films [53]. Among the other four identified states, only two exhibit topological textures. These are (5) the I-meron bubble state with an intermediate helicity $\gamma \approx -3\pi/4$ between Bloch- and Néel-type merons and with skyrmion number $N_{sk} = \frac{1}{2}$ [Fig. 2(c)] forming in a small tensile strain area [orange area in Fig. 2(a)] and (6) the bobber-shaped meron bubble pair [meron pair, yellow area in Fig. 2(a)] composed of two types of I-meron structures aligned along the z axis, as shown in Fig. 2(c), which

depends on larger tensile strains, resulting in more rotated P_{ip}. In the I-meron case, the volume fraction of the c domains is ∼0.5, whereas the domain orientations and shapes predicted from modeling agree well with existing experimental observations under tensile strains [20,54]. Meanwhile, the other two identified states are (7) the c/a funnel state that exhibits a trianglelike c or a domain at the cross-section, with the case of $\varepsilon_{11} = 0.2\%$ mismatch strain shown in Fig. 3(b) and its ρ shown in Fig. 3(f) and (8) the c/a bowl state, which is like the c/a funnel state and possesses an out-of-plane nanobowl at the cross-section, occurring only under large thickness.

The states along path 1 at 8 u.c. in Fig. 2(a) undergo a transformation from c stripe, c/a funnel, I-meron to meron pair, ultimately leading to the emergence of the a_1/a_2 domain. During these transformations, P_{op} continuously shifts to P_{ip}, resulting in the formation of various distinct domains. The domain walls transition from the 180° ultra-narrow domain walls between c domains to 90° domain walls between c and a domains under strains ranging from $\varepsilon_{11} = -1$ to 0.2%, as shown in Figs. 3(a) and 3(b). With increasing P_{ip}, as shown in Figs. 3(b) and 3(c), some complex textures appeared with mixing $a_1(a_2)$ as c domains. Interestingly, Néel-type domain walls gradually transition to mixing Néel- and Bloch-type domain walls at $\varepsilon_{11} = 0.5\%$. These two distinct types of domain walls are balanced in ultrathin films, forming a I-meron and meron pair, as shown in Figs. 3(c) and 3(d) under $\varepsilon_{11} = 0.5$ and 1%, respectively. In Figs. 3(d) and 3(h), there are two regions with the same topological charges $N_{sk} = \frac{1}{2}$ represented by blue and red circles. However, they exhibit clockwise or counterclockwise vortices surrounding P_{op} for opposite chiralities, respectively. The evolutionary details and zoom-in map, illustrating the transition from the I-meron bubble to the meron pair bubble, are depicted in Fig. S2 in the Supplemental Material [50]. On the other hand, along path 2 with increasing film thickness under strain $\varepsilon_{11} = 0.6\%$, five configurations are observed. The states vary from a_1/a_2, meron pair, I-meron,
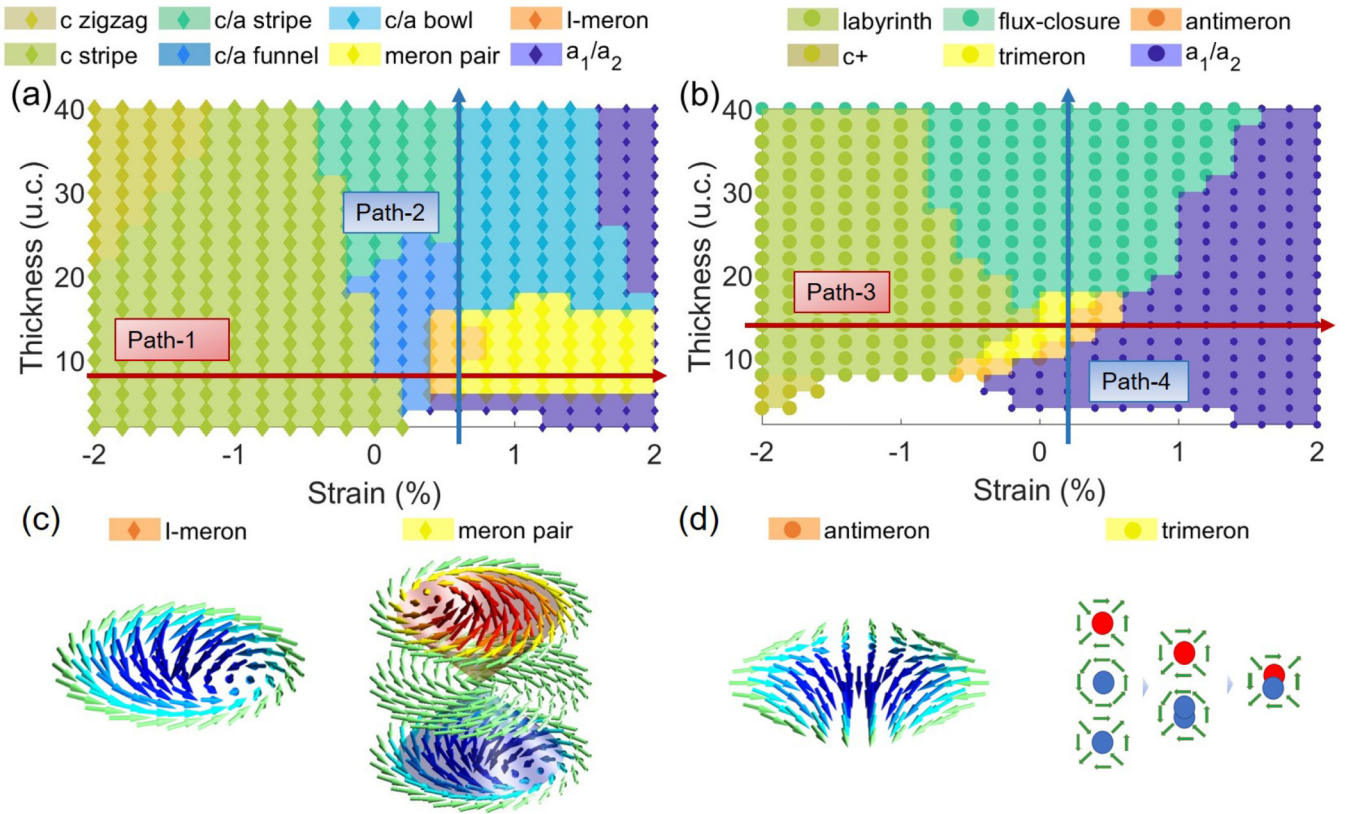
FIG. 2. Phase diagram in the parameter space defined by the thickness and epitaxial strain of PZT film under (a) short-circuit (sc) and (b) open-circuit (oc) electrical boundary conditions, simulated by the phase-field modeling approach. In (a), there are eight phases: c zigzag domain (c zigzag), c stripe, a_1 (a_2) stripe domain insert in c domain (c/a stripe), c domain or a_1 (a_2) domain like a funnel at the across section (c/a funnel), bowl-shaped c domain insert a_1 (a_2) domain (c/a bowl), bobber-shaped meron bubble pair (meron pair), intermediate meron bubble (I-meron), and a_1 and a_2 stripe domain (a_1/a_2). In (b), there are six phases: labyrinth phase (labyrinth), $c+$ domain ($c+$), flux closure, trimeron bubble, antimeron bubble, and a_1 and a_2 stripe domain (a_1/a_2). The different colors show distinct textures, and at the boundaries of color areas, phase mixing occurs. Paths 1 and 3 are along the varied strains at 8 and 14 u.c., respectively. Paths 2 and 4 are along the different thicknesses under 0.6 and 0.2% strains, respectively. The white area in (a) and (b) designates nonferroelectric state as shown in Fig. S1(b1) in the Supplemental Material [50]. (c) Two polar textures of I-meron and meron pair under sc boundary conditions. (d) Two polar textures of antimeron and trimeron under oc boundary conditions.

c/a funnel to c/a stripe (see Fig. S3 in the Supplemental Material [50]). With increasing h, there is a gradual increase of P_{op}. Consequently, the meron pair and I-meron bubble phases (Figs. S3(b) and S3(c) in the Supplemental Material [50]) appear in the film. The proportion of the c domains gradually increases as h increases, resulting in the texture of the c/a funnel (Fig. S3(d) in the Supplemental Material [50] and c/a stripe (Fig. S3(e) in the Supplemental Material [50]).

We also compare different energy terms and analyze which favor stability of the ferroelectric topological polar phase (see Fig. S4 in the Supplemental Material [50]). In Fig. S4(a) in the Supplemental Material [50] along path 1, the strain varies from −2 to 2%. The formation of stripe domains is primarily dominated by the elastic energy due to large compressive strain. As the magnitude of strain decreases, the elastic energy gradually decreases, while the electric energy and gradient energy become increasingly dominant, leading to an augmented in-plane polarization. When the strain is ∼0–1%, a reduction in the gradient energy favors the formation of twisted vortices with rotational polarization, resulting in the emergence of I-meron and meron pair phases. Eventually, the formation of

a_1/a_2 under a large tensile strain is owing to the increasing elastic energy which also remained vortices in-plane. The Landau free energy is observed to be zero when the film thickness is too thin, ∼2 u.c., at a tensile strain of 0.6%, as depicted in Fig. S4(b) in the Supplemental Material [50]. It should be noted that, under these conditions, the formation of ordered ferroelectric domains is not possible.

We next examine the results under the oc boundary condition. As shown in Fig. 2(b), there are six states in the h-S phase diagram. Among these, four states have already been reported in PZT films and $[PZT]_n/[STO]_n$ superlattice [28]. When $h < 8$ u.c., topologically trivial polar structures [55], such as c_+ single-domain even paraelectric states, dominate due to the large depolarization field in ultrathin films. The other three previously known states are (1) the labyrinth state, with a domain for a mismatch strain of $\varepsilon_{11} = −1\%$ shown in Fig. 4(a), wherein the state includes individual skyrmion bubble [Figs. 1(a)–1(d)] and polar spiral tubes. The curl of in-plane polarization is shown in Fig. S5 in the Supplemental Material [50]. The topological characters are shown in Fig. 4(e) for high compressive strains at small film
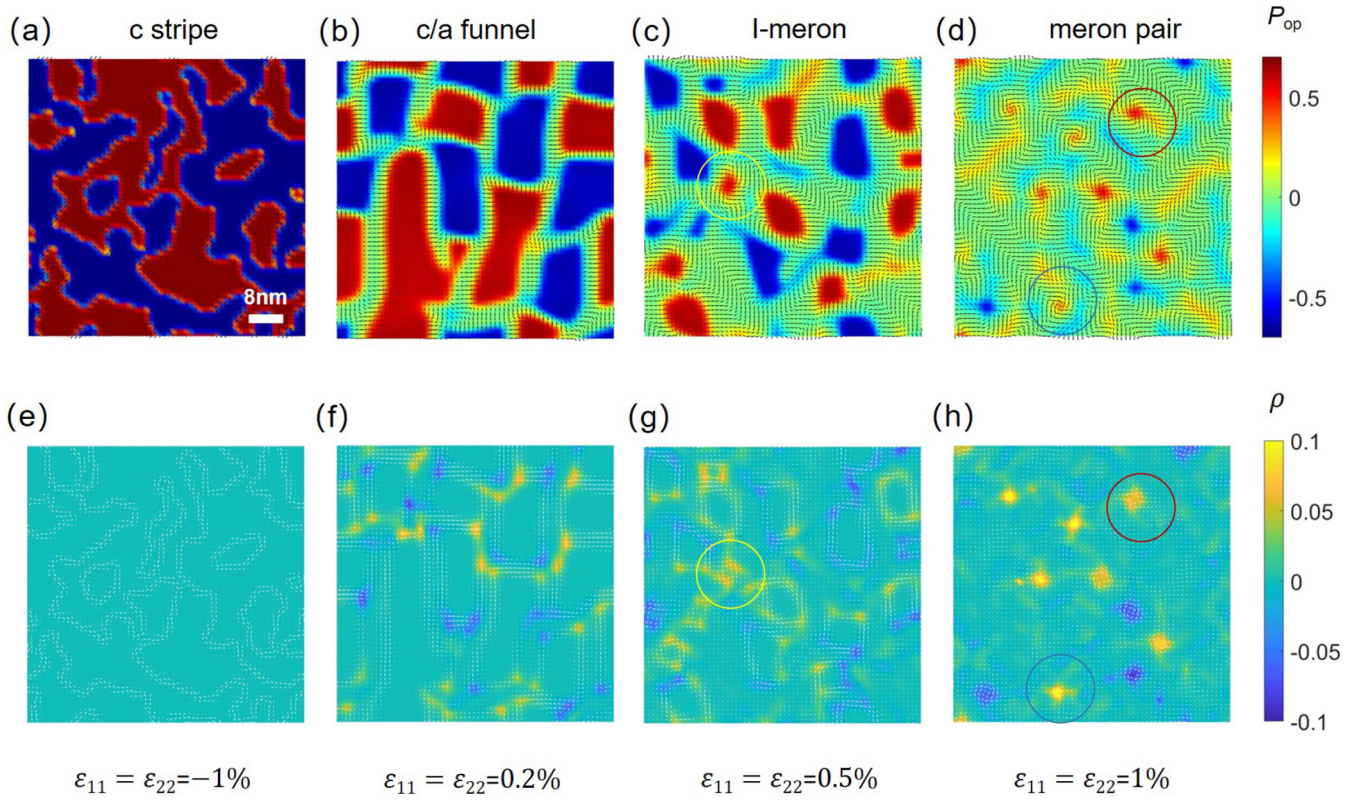
FIG. 3. (a)–(d) Polarization vector and (e)–(h) Pontryagin density maps for the c stripe, c/a funnel, I-meron, and meron pair phases under varied strain for 8 u.c. (~3.2 nm) thin film along path 1 defined in Fig. 2(a). The black and white arrows show the in-plane polarization and the curl of polarization (P), respectively. These maps depict the spatial distribution of polarization in the cross-section (001) plane, showcasing the variation of the topological textures under different conditions.
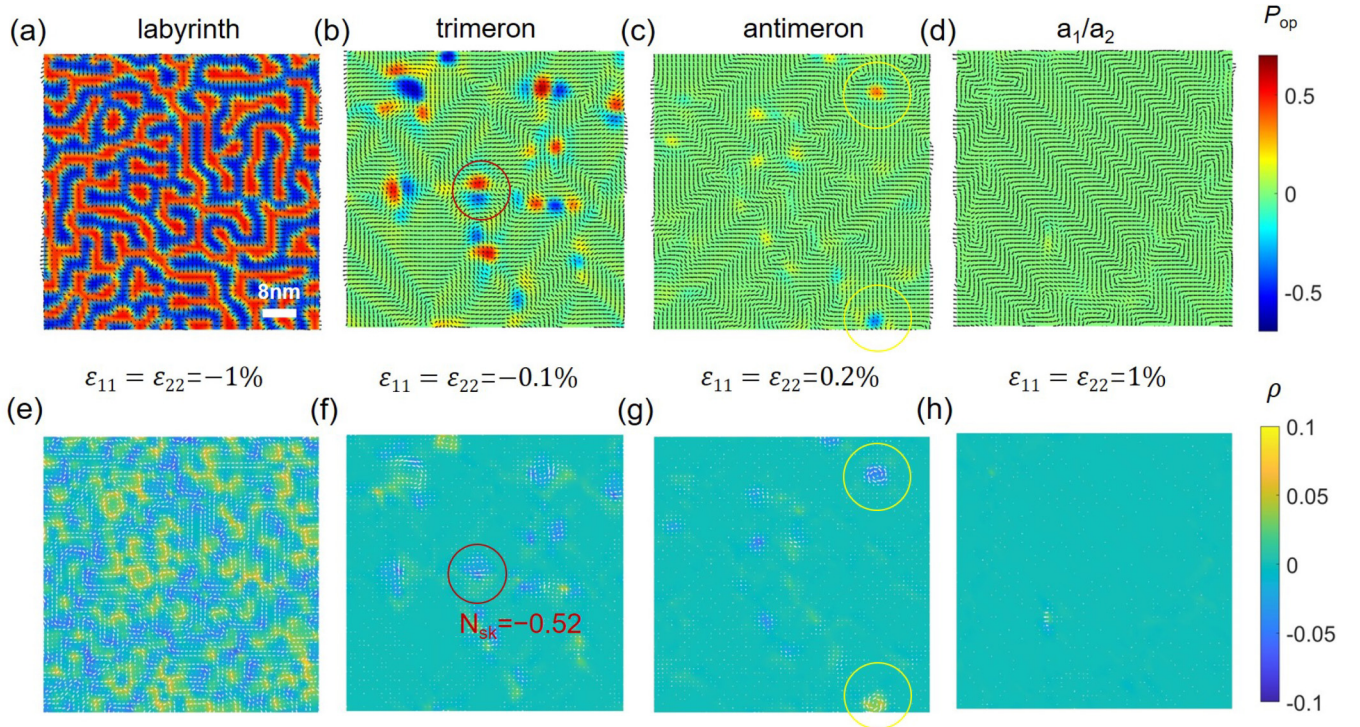

FIG. 4. (a)–(d) Polarization vector and (e)–(h) Pontryagin density maps for the labyrinth, trimeron, antimeron, and a_1/a_2 topological textures under varied strains for 14 u.c. (~5.6 nm) thin film along path 3 defined in Fig. 2(b). The black and white arrows show the in-plane polarization and the curl of polarization (P), respectively.

thicknesses, corresponding to $[PTO]_n/[STO]_n$ superlattice and $[PTO]_n/[STO]_m$ thin films [18,55]. (2) The flux-closure state is observed in PZT bulk or thick films without strain [11]. Three-dimensional effects become more prominent, causing the a_1 or a_2 domain to preferentially turn by $90°$. The c domain appears in the bulk of the film, while the a_1/a_2 domain remains on the surface. In previous works, the periodic wave flux-closure domain appeared during heating-cooling cycles, forming the stripe phase turned into the periodic wave flux-closure phase [13,37]. (3) The a_1/a_2 stripe state appears under large tensile strains like the case under the sc boundary condition, and a_1 and a_2 domains dominate with $90°$ domain walls, as shown in Fig. 4(d). The other two identified states are antimeron and trimeron states, which are denoted by a_1/a_2 and c domains with small orange and yellow areas in Fig. 2(b), respectively. We define meron or antimeron according to their winding numbers. For an antimeron, as shown in Fig. 2(d), it has achiral structures [24], and this texture appears under small tensile strains ($\varepsilon_{11} = 0.2\%$) and small film thicknesses ($h = 14$ u.c.), as shown in Fig. 4(c) in the yellow circle, and its $\rho \sim 0.1$, as shown in Fig. 4(g). Meanwhile, the trimeron bubble consists of two antimeron bubbles and one Bloch-like meron bubble with different topological characteristics, where the hypothetical combination process is shown in Fig. 2(d). The domain structure exhibits under a mismatch strain of $\varepsilon_{11} = -0.1\%$, as shown in Fig. 4(b). The volume fraction of the a_1/a_2 domain is ~ 0.9. The horizontal cross-section [Fig. 4(b)] and its corresponding topological density map [Fig. 4(f)] clearly show that this structure can be divided into two parts: the P_{op} up part features with a half-convergent-half-divergent configuration with negative topological density and negative winding number (antimeron), while the P_{op} down part features are divided with an anticlockwise configuration with negative topological density and a half-convergent-half-divergent configuration with positive topological density. The trimeron texture has a topological charge of -0.52, as shown by the red circle in Fig. 4(f). The P_{op} down part feature is the so-called topological trivial meron pair (TTMP [25]) or meron-antimeron combination (MAC [20]) with zero topological charge. Other trimeron structures are depicted in Figs. S6 and S7(c) in the Supplemental Material [50].

According to the phase diagram shown in Fig. 2(b), along path 3 with the change of strain, the states vary from labyrinth, trimeron, antimeron to a_1/a_2. Interestingly, the trimeron state containing a meron and antimeron changes to the single meron state, as shown in Figs. 4(b) and 4(c), under strain from $\varepsilon_{11} = -0.1$ to 0.2% under 14 u.c. film thickness. The evolution from the trimeron phase to the antimeron phase, along with corresponding sketches shown in Fig. S6 in the Supplemental Material [50], provides a detailed analysis. The out-of-plane polarization completely rotates to in-plane with increasing strain, as shown in Fig. 4(d). Meanwhile, along path 4 with increasing film thickness under strain $\varepsilon_{11} = 0.2\%$, as shown in Fig. S7 in the Supplemental Material [50], four configurations are observed. The states vary from a_1/a_2, antimeron, trimeron to flux-closure. When $h < 12$ u.c., only a_1/a_2 domains are present in the thin film, resulting in a_1/a_2 vortex in the plane. When h reaches 12 u.c., the c domains emerge gradually, forming a antimeron and trimeron, and then the meron-related

states are replaced by flux closure with further increasing of the film thickness.

The different energy terms of ferroelectric polar phase along path 3 are shown in Fig. S4(c) in the Supplemental Material [50]; the formation of labyrinth domains is primarily influenced by the increase in elastic and electric energy resulting from significant compressive strains ($\varepsilon_{11} < -1.2\%$). As the magnitude of strain decreases, the elastic energy gradually decreases, while the electric energy and gradient energy become increasingly dominant, leading to an augmented proportion of in-plane polarization. When the strain is between -0.2 and 0.4%, a reduction gradient energy leads to the formation of vortices with rotational in-plane polarization. The vortice and antivortice in-plane coexistence of P_{op} leads to the trimeron and antimeron phases. Eventually, the formation of a_1/a_2 with in-plane polarization under a large tensile strain is owing to the increasing elastic energy. The compared different energy terms along path 4 of thickness are shown in Fig. S4(d) in the Supplemental Material [50].

C. Polar meron pairs

Meron bobber pair structures have been previously reported in both theoretical and experimental studies [27,56–58] at composite magnetic disks and thick extended films of noncentrosymmetric ferromagnets. Polar textures also have potential as applications in next-generation electronic devices [3]. However, analogous meron bobber pair structures have not been reported in ferroelectric materials.

According to the h-S phase diagram, the meron pair phase occurs only in the strain range of 0.6–2%. The meron pair under tensile strain (1%) and with thickness of 8 u.c. (~ 3.2 nm) is shown in Fig. 5(a), where P_{op} is up (red) and down (blue) in q and m points, respectively. Figure 5(a) shows P_{ip} with a green arrow, while up P_{op} is a red arrow and down P_{op} is a blue arrow. The shapes of the meron pair resemble two bobbers in the longitudinal cross-section [see the right panel of Fig. 5(a)].

Selected maps of top, middle, and bottom layers around the q and m points in red and blue boxes are shown in Figs. 5(b) and 5(c). The P_{op} regions at meron cores and outside the boundary are indicated by the colored regions, which are separated by mixing Bloch and Néel domain walls (P_{ip}). The P_{ip} (± 0.3 C/m^2) around P_{op} (± 0.5 C/m^2) is shown as counterclockwise or clockwise vortices composed of merons. The size of the meron pair is 8 nm. All top-, middle-, and bottom-layer vortices are converged with counterclockwise rotation from the periphery to the central regions, yielding a vorticity of $+1$ and helicity of $3\pi/4$ at q position, as shown in Fig. 5(b). Combining P_{ip} and P_{op}, a meron manifests a skyrmion number of $N_{sk} = \frac{1}{2}$ at the top layer and $N_{sk} = -\frac{1}{2}$ at the bottom layer. Two inversion chiral I-merons with $N_{sk} = \pm\frac{1}{2}$, vorticity $m = +1$, and helicity $\gamma = 3\pi/4$ type are aligned along the z axis to form a convergent meron pair. Here, P_{ip} evolves counterclockwise around the core P_{op}. Also, P_{op} has inversion symmetry and takes a shape like a diabolo (two bobbers), as shown in Fig. 5(d). The range of the c domain on the top surface is large, becomes smaller on the middle, and gradually shifts direction of polarization on the bottom. The P_{op} components vanish in the middle layer, remaining only as a counterclockwise twist vortex. Meanwhile, for the divergent meron pair at the
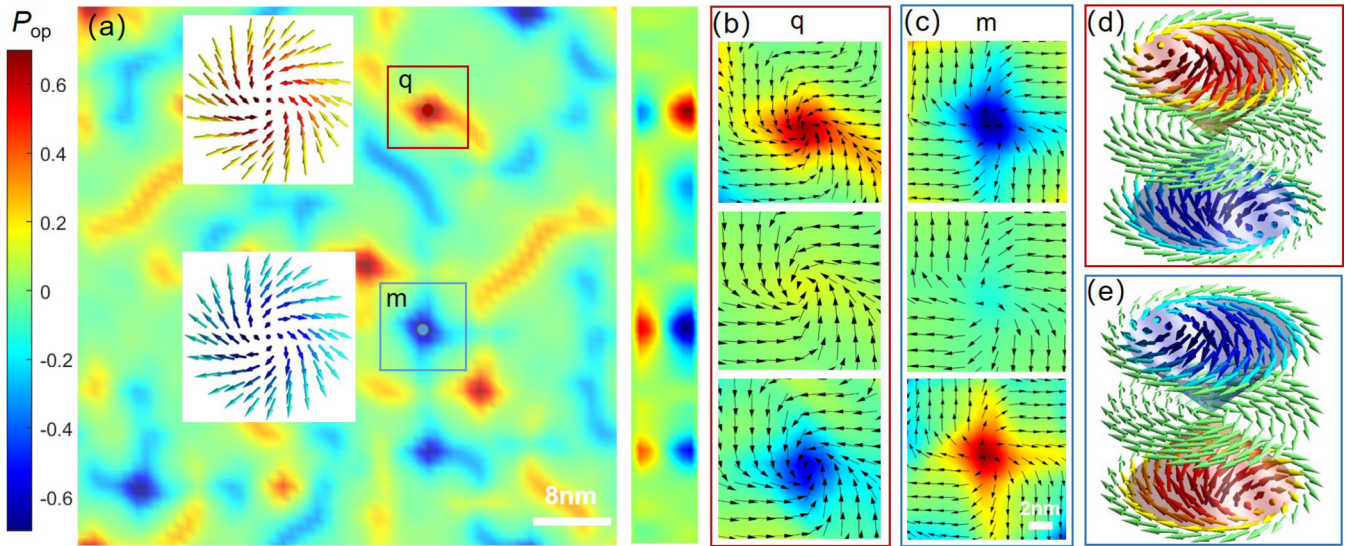
FIG. 5. Simulated polar meron bubble pair for 8 u.c. PZT thin film under 1% strain. (a) The topological texture on the top layer (left side) with the cross-sectional view along q and m positions (right side). Inset shows images of two types of I-meron. (b) and (c) A zoom-in view of the meron with in-plane and across the plane at q and m positions, on the top, middle, and bottom layers, respectively. Red area has up P_{op} and blue area has down P_{op}. The black arrows indicate P_{ip}. (d) and (e) The converged and diverged diabolo-shaped meron pair. The arrow and area indicate the polar vector and cross-sections of the corresponding isosurfaces ($P_{op} = 0$).

m position, all top-, middle-, and bottom-layer vortices are diverged and undergo clockwise rotation from the periphery to the central regions, yielding a vorticity of $+1$ and helicity of $-\pi/4$, as shown in Fig. 5(c) with meron characters $N_{sk} = \pm\frac{1}{2}$, vorticity $m = +1$, and helicity $\gamma = -\pi/4$. Here, P_{op} possesses inversion symmetry and adopts a diabolo shape, as shown in Fig. 5(e), analogous to those in composite magnetic disks [27,56].

IV. SUMMARY

Based on extensive phase-field modeling simulations, we have constructed comprehensive phase diagrams for polar topological textures in the parameter space of film thickness and strain in PZT thin film under the sc and oc boundary conditions. Our results reproduce and confirm previously reported findings and reveal additional topological phases with complex polar textures. A distinct polar topology, namely, the meron bubble pair, is observed in ultrathin films below a critical thickness, while thicker films exhibit more complex domain structures. Overall, the tunability of two nontrivial topological phases, namely, the I-meron and meron pair phases (or antimeron and trimeron phases), in sc (or oc) boundary conditions is achieved through strain manipulation within a critical thickness range of 6–18 u.c. (or 8–18 u.c.). For ultrathin ferroelectric films, domain structures are significantly different under distinct boundary conditions. With the control of decreasing film thickness, topological textures can be tailored to transition from achiral merons to chiral convergent/divergent meron pairs. Merons and their variants can emerge as individual or mixing polar spin

textures. These findings offer insights into understanding the complex topological structures in an important class of materials, which may help further exploration and utilization of polar meron-related structures to drive exciting advances in material physics research and stimulate promising device applications.

For practical applications, it is extremely important to manipulate the size and morphology of the topological textures and control their generation and annihilation in a convenient and low-dissipation way. Previous researchers were primarily focused on skyrmion-related objects, while other meron-related structures were ignored. Our simulations exhibit continuous changes over a wide range, not limited to discrete values, providing further regulation of meron and meron-related texture transformation. The phase diagrams and the evolution from each phase in this paper can give deep insight into control of the polarization texture generation and annihilation.

[1] S. Chen, S. Yuan, Z. Hou, Y. Tang, J. Zhang, T. Wang, K. Li, W. Zhao, X. Liu, L. Chen *et al.*, Recent progress on topological structures in ferroic thin films and heterostructures, Adv. Mater. **33**, e2000857 (2021).

[2] Z. Liu, H. Wang, M. Li, L. Tao, T. R. Paudel, H. Yu, Y. Wang, S. Hong, M. Zhang, Z. Ren *et al.*, In-plane charged domain walls with memristive behaviour in a ferroelectric film, Nature (London) **613**, 656 (2023).

[3] L. Han, C. Addiego, S. Prokhorenko, M. Wang, H. Fu, Y. Nahas, X. Yan, S. Cai, T. Wei, Y. Fang *et al.*, High-density switchable skyrmion-like polar nanodomains integrated on silicon, Nature (London) **603**, 63 (2022).

[4] J. Yang, Y. Zou, W. Tang, J. Li, M. Huang, and S. Aya, Spontaneous electric-polarization topology in confined ferroelectric nematics, Nat. Commun. **13**, 7806 (2022).

[5] D. Karpov, Z. Liu, T. d. S. Rolo, R. Harder, P. V. Balachandran, D. Xue, T. Lookman, and E. Fohtung, Three-dimensional imaging of vortex structure in a ferroelectric nanoparticle driven by an electric field, Nat. Commun. **8**, 280 (2017).

[6] D. Liu, J. Wang, H. M. Jafri, X. Wang, X. Shi, D. Liang, C. Yang, X. Cheng, and H. Huang, Phase-field simulations of vortex chirality manipulation in ferroelectric thin films, npj Quantum Mater. **7**, 34 (2022).

[7] Z. Hong, A. R. Damodaran, F. Xue, S. L. Hsu, J. Britson, A. K. Yadav, C. T. Nelson, J. J. Wang, J. F. Scott, L. W. Martin *et al.*, Stability of polar vortex lattice in ferroelectric superlattices, Nano Lett. **17**, 2246 (2017).

[8] Y. Li, Y. Jin, X. Lu, J. C. Yang, Y. Chu, F. Huang, J. Zhu, and S. W. Cheong, Rewritable ferroelectric vortex pairs in BiFeO$_3$, npj Quantum Mater. **2**, 43 (2017).

[9] A. Y. Abid, Y. Sun, X. Hou, C. Tan, X. Zhong, R. Zhu, H. Chen, K. Qu, Y. Li, M. Wu *et al.*, Creating polar antivortex in PbTiO$_3$/SrTiO$_3$ superlattice, Nat. Commun. **12**, 2054 (2021).

[10] Y. J. Wang, Y. L. Tang, Y. L. Zhu, and X. L. Ma, Entangled polarizations in ferroelectrics: A focused review of polar topologies, Acta Mater. **243**, 118485 (2023).

[11] C. L. Jia, K. W. Urban, M. Alexe, D. Hesse, and I. Vrejoiu, Direct observation of continuous electric dipole rotation in flux-closure domains in ferroelectric Pb(Zr, Ti)O$_3$, Science **331**, 1420 (2011).

[12] Y. L. Tang, Y. L. Zhu, X. L. Ma, A. Y. Borisevich, A. N. Morozovska, E. A. Eliseev, W. Y. Wang, Y. J. Wang, Y. B. Xu, Z. D. Zhang *et al.*, Ferroelectrics. observation of a periodic array of flux-closure quadrants in strained ferroelectric PbTiO$_3$ films, Science **348**, 547 (2015).

[13] W. R. Geng, X. Guo, H. L. Ge, Y. L. Tang, Y. Zhu, Y. Wang, B. Wu, M. J. Zou, Y. P. Feng, and X. L. Ma, Real-time transformation of flux-closure domains with superhigh thermal stability, Nano Lett. **22**, 8892 (2022).

[14] S. Das, Y. L. Tang, Z. Hong, M. A. P. Goncalves, M. R. McCarter, C. Klewe, K. X. Nguyen, F. Gomez-Ortiz, P. Shafer, E. Arenholz *et al.*, Observation of room-temperature polar skyrmions, Nature (London) **568**, 368 (2019).

[15] Y. Zhang, Q. Li, H. Huang, J. Hong, and X. Wang, Strain manipulation of ferroelectric skyrmion bubbles in a freestanding PbTiO$_3$ film: A phase field simulation, Phys. Rev. B **105**, 224101 (2022).

[16] Y. Nahas, S. Prokhorenko, L. Louis, Z. Gui, I. Kornev, and L. Bellaiche, Discovery of stable skyrmionic state in ferroelectric nanocomposites, Nat. Commun. **6**, 8542 (2015).

[17] X. R. Wang, X. C. Hu, and H. T. Wu, Stripe skyrmions and skyrmion crystals, Commun. Phys. **4**, 142 (2021).

[18] Z. Hong and L.-Q. Chen, Blowing polar skyrmion bubbles in oxide superlattices, Acta Mater. **152**, 155 (2018).

[19] Y. T. Shao, S. Das, Z. Hong, R. Xu, S. Chandrika, F. Gomez-Ortiz, P. Garcia-Fernandez, L. Q. Chen, H. Y. Hwang, J. Junquera *et al.*, Emergent chirality in a polar meron to skyrmion phase transition, Nat. Commun. **14**, 1355 (2023).

[20] Y. J. Wang, Y. P. Feng, Y. L. Zhu, Y. L. Tang, L. X. Yang, M. J. Zou, W. R. Geng, M. J. Han, X. W. Guo, B. Wu *et al.*, Polar meron lattice in strained oxide ferroelectrics, Nat. Mater. **19**, 881 (2020).

[21] N. Nagaosa and Y. Tokura, Topological properties and dynamics of magnetic skyrmions, Nat. Nanotechnol. **8**, 899 (2013).

[22] X. Z. Yu, W. Koshibae, Y. Tokunaga, K. Shibata, Y. Taguchi, N. Nagaosa, and Y. Tokura, Transformation between meron and skyrmion topological spin textures in a chiral magnet, Nature (London) **564**, 95 (2018).

[23] B. Göbel, I. Mertig, and O. A. Tretiakov, Beyond skyrmions: Review and perspectives of alternative magnetic quasiparticles, Phys. Rep. **895**, 1 (2021).

[24] B. Göbel, A. Mook, J. Henk, I. Mertig, and O. A. Tretiakov, Magnetic bimerons as skyrmion analogues in in-plane magnets, Phys. Rev. B **99**, 060407(R) (2019).

[25] H. Jani, J. C. Lin, J. Chen, J. Harrison, F. Maccherozzi, J. Schad, S. Prakash, C. B. Eom, A. Ariando, T. Venkatesan *et al.*, Antiferromagnetic half-skyrmions and bimerons at room temperature, Nature (London) **590**, 74 (2021).

[26] J. Sun, S. Shi, Y. Wang, and J. Wang, Phase field modeling of topological magnetic structures in ferromagnetic materials: Domain wall, vortex, and skyrmion, Acta Mech. **234**, 283 (2023).

[27] C. Phatak, A. K. Petford-Long, and O. Heinonen, Direct observation of unconventional topological spin structure in coupled magnetic discs, Phys. Rev. Lett. **108**, 067205 (2012).

[28] R. Zhu, Z. Jiang, X. Zhang, X. Zhong, C. Tan, M. Liu, Y. Sun, X. Li, R. Qi, K. Qu *et al.*, Dynamics of polar skyrmion bubbles under electric fields, Phys. Rev. Lett. **129**, 107601 (2022).

[29] K. Du, M. Zhang, C. Dai, Z. N. Zhou, Y. W. Xie, Z. H. Ren, H. Tian, L. Q. Chen, G. Van Tendeloo, and Z. Zhang, Manipulating topological transformations of polar structures through real-time observation of the dynamic polarization evolution, Nat. Commun. **10**, 4864 (2019).

[30] A. R. Damodaran, J. D. Clarkson, Z. Hong, H. Liu, A. K. Yadav, C. T. Nelson, S. L. Hsu, M. R. McCarter, K. D. Park, V. Kravtsov *et al.*, Phase coexistence and electric-field control of toroidal order in oxide superlattices, Nat. Mater. **16**, 1003 (2017).

[31] J. Hlinka, V. Stepkova, P. Marton, I. Rychetsky, V. Janovec, and P. Ondrejkovic, Phase-field modelling of 180° "Bloch walls" in rhombohedral BaTiO$_3$, Phase Transit. **84**, 738 (2011).

[32] D. Liang, X. Ma, Z. Liu, H. M. Jafri, G. Cao, H. Huang, S. Shi, and L.-Q. Chen, Phase-field simulation of two-dimensional topological charges in nematic liquid crystals, J. Appl. Phys. **128**, 124701 (2020).

[33] F. H. Gong, Y. T. Chen, Y. L. Zhu, Y. L. Tang, H. Zhang, Y. J. Wang, B. Wu, J. Q. Liu, T. T. Shi, L. X. Yang *et al.*, Thickness-dependent polar domain evolution in strained, ultrathin PbTiO$_3$ films, ACS Appl. Mater. Interfaces **14**, 9724 (2022).

[34] X. Wang, Y.-C. Wang, B. Peng, J. Deng, Y. Yang, W. Sun, and Z. Wang, Thickness dependence of PbZr$_{0.52}$Ti$_{0.48}$O$_3$ thin film ferroelectric parameters, Nano Energy **107**, 108161 (2023).

[35] A. R. Damodaran, S. Pandya, J. C. Agar, Y. Cao, R. K. Vasudevan, R. Xu, S. Saremi, Q. Li, J. Kim, M. R. McCarter *et al.*, Three-state ferroelastic switching and large

electromechanical responses in PbTiO$_3$ thin films, Adv. Mater. **29**, 1702069 (2017).

[36] D. Sichuga and L. Bellaiche, Epitaxial Pb(Zr, Ti)O$_3$ ultrathin films under open-circuit electrical boundary conditions, Phys. Rev. Lett. **106**, 196102 (2011).

[37] X. Li, C. Tan, C. Liu, P. Gao, Y. Sun, P. Chen, M. Li, L. Liao, R. Zhu, J. Wang *et al.*, Atomic-scale observations of electrical and mechanical manipulation of topological polar flux closure, Proc. Natl. Acad. Sci. USA **117**, 18954 (2020).

[38] P. Behera, M. A. May, F. Gómez-Ortiz, S. Susarla, S. Das, C. T. Nelson, L. Caretta, S.-L. Hsu, M. R. McCarter, B. H. Savitzky *et al.*, Electric field control of chirality, Sci. Adv. **8**, eabj8030 (2022).

[39] M. J. Haun, E. Furman, S. J. Jang, and L. E. Cross, Thermodynamic theory of the lead zirconate-titanate solid solution system, part I: Phenomenology, Ferroelectrics **99**, 13 (1989).

[40] A. Amin, M. J. Haun, B. Badger, H. McKinstry, and L. E. Cross, A phenomenological Gibbs function for the single cell region of the PbZrO$_3$: PbTiO$_3$ solid solution system, Ferroelectrics **65**, 107 (1985).

[41] S. Nambu and D. A. Sagala, Domain formation and elastic long-range interaction in ferroelectric perovskites, Phys. Rev. B **50**, 5838 (1994).

[42] Y. L. Li, S. Y. Hu, Z. K. Liu, and L. Q. Chen, Phase-field model of domain structures in ferroelectric thin films, Appl. Phys. Lett. **78**, 3878 (2001).

[43] Y. L. Li, L. Q. Chen, G. Asayama, D. G. Schlom, M. A. Zurbuchen, and S. K. Streiffer, Ferroelectric domain structures in epitaxial thin films: Electron microscopy and phase-field simulations, J. Appl. Phys. **95**, 6332 (2004).

[44] Y. L. Li, S. Y. Hu, Z. K. Liu, and L. Q. Chen, Effect of electrical boundary conditions on ferroelectric domain structures in thin films, Appl. Phys. Lett. **81**, 427 (2002).

[45] L. Q. Chen and J. Shen, Applications of semi-implicit fourier-spectral method to phase field equations, Comput. Phys. Commun. **108**, 147 (1998).

[46] Z. Gu, S. Pandya, A. Samanta, S. Liu, G. Xiao, C. J. G. Meyers, A. R. Damodaran, H. Barak, A. Dasgupta, S. Saremi *et al.*, Resonant domain-wall-enhanced tunable microwave ferroelectrics, Nature (London) **560**, 622 (2018).

[47] D. Liu, J. Wang, J. S. Wang, and H. B. Huang, Phase field simulation of misfit strain manipulating domain structure and ferroelectric properties in PbZr$_{(1-x)}$Ti$_x$O$_3$ thin films, Acta Phys. Sin. **69**, 127801 (2020).

[48] J. Hlinka, Mobility of ferroelastic domain walls in barium titanate, Ferroelectrics **349**, 49 (2007).

[49] S. W. Cheong and X. Xu, Magnetic chirality, npj Quantum Mater. **7**, 40 (2022).

[50] See Supplemental Material at http://link.aps.org/supplemental/10.1103/PhysRevB.109.094116 for domain configurations on a zero strain ($\varepsilon_{11} = \varepsilon_{22} = 0.0\%$) from 2 to 39 u.c. (Fig. S1); the evolution of polarizations from I-meron phase to meron pair phase (Fig. S2); the textures along path 2, characterization of labyrinth phases, and typical evolution processes of topological phase transitions with thickness (Fig. S3); the evolution of different energy components with respect to thickness and strain (Fig. S4); the polar skyrmion bubbles in labyrinth phase (Fig. S5); the evolution of polarizations from trimeron phase to antimeron phase (Fig. S6); and the evolution processes of textures along path 4 with varying thicknesses (Fig. S7), which includes Refs. [9,42,51,59].

[51] S. K. Streiffer, J. A. Eastman, D. D. Fong, C. Thompson, A. Munkholm, M. V. Ramana Murty, O. Auciello, G. R. Bai, and G. B. Stephenson, Observation of nanoscale 180 degrees stripe domains in ferroelectric PbTiO$_3$ thin films, Phys. Rev. Lett. **89**, 067601 (2002).

[52] G. De Luca, M. D. Rossell, J. Schaab, N. Viart, M. Fiebig, and M. Trassin, Domain wall architecture in tetragonal ferroelectric thin films, Adv. Mater. **29**, 1605145 (2017).

[53] F. Xue, J. J. Wang, G. Sheng, E. Huang, Y. Cao, H. H. Huang, P. Munroe, R. Mahjoub, Y. L. Li, V. Nagarajan *et al.*, Phase field simulations of ferroelectrics domain structures in PbZr$_x$Ti$_{1-x}$O$_3$ bilayers, Acta Mater. **61**, 2909 (2013).

[54] Y. J. Wang, Y. L. Tang, Y. L. Zhu, and X. L. Ma, Meron-antimeron annihilation induced by the electric field in a polar meron lattice, J. Appl. Phys. **131**, 224102 (2022).

[55] S. Yuan, Z. Chen, S. Prokhorenko, Y. Nahas, L. Bellaiche, C. Liu, B. Xu, L. Chen, S. Das, and L. W. Martin, Hexagonal close-packed polar-skyrmion lattice in ultrathin ferroelectric PbTiO$_3$ films, Phys. Rev. Lett. **130**, 226801 (2023).

[56] S. Wintz, C. Bunce, A. Neudert, M. Korner, T. Strache, M. Buhl, A. Erbe, S. Gemming, J. Raabe, C. Quitmann *et al.*, Topology and origin of effective spin meron pairs in ferromagnetic multilayer elements, Phys. Rev. Lett. **110**, 177201 (2013).

[57] P. S. Amit and H. Riccardo, Three-dimensional chiral magnetization structures in FeGe nanospheres, Phys. Rev. B **103**, 104414 (2021).

[58] F. N. Rybakov, A. B. Borisov, S. Blugel, and N. S. Kiselev, New type of stable particlelike states in chiral magnets, Phys. Rev. Lett. **115**, 117201 (2015).

[59] J. Wang, M. Kamlah, and T.-Y. Zhang, Phase field simulations of low-dimensional ferroelectrics, Acta Mech. **214**, 49 (2010).